Oil Shale, 2026, 43, 2, 117–142 https://doi.org/10.3176/oil.2026.2.01

Numerical investigation of oil shale combustion characteristics in a high-low differential velocity CFB boiler using the CPFD model

Hongpeng Liu[(a)], Xuexin Xiang[(a)], Shichao Li[(a)], Shuaishuai Cui[(a)], Chunxia Jia[(a)]*, Hong Qin[(a)], Qing Wang[(a)], Mingzhi Shan[(b)], Bin Liu[(b)], Wen Yang[(c)]

[(a)] Engineering Research Center of Oil Shale Comprehensive Utilization, Ministry of Education, School of Energy and Power Engineering, Northeast Electric Power University, 169 Changchun Road, Jilin 132012, China
[(b)] Victory Shale Oil Retorting Experimental Plant, Fushun Mining Group Co. Ltd., North side of Nanhuang Road, Fushun 113000, China
[(c)] Jiangxi Jianglian Heavy Industry Group Co. Ltd., 999 Aixihu Fourth Road, Nanchang 330000, China

Received 28 September 2025, accepted 8 April 2026, available online 16 April 2026

Abstract. *This study employs the computational particle fluid dynamic model to simulate a 65 t/h oil shale-fired high-low differential velocity circulating fluidized bed (CFB) boiler. The effects of the excess air ratio on furnace temperature, gas composition, particle residence time, and pollutant emissions were analyzed. Results show that an excess air ratio of 1.10 intensifies particle back-mixing, enhancing combustion while reducing NO and SO_2 emissions. The optimal condition combines this ratio with a 1.5:1 main/side bed air distribution, achieving the lowest emissions. This work provides valuable insights for optimizing CFB boiler operation.*

Keywords: *oil shale, high-low differential velocity CFB, gas-solid flow, combustion characteristics, gas pollutants, computational particle fluid dynamics.*

1. Introduction

The high-low differential velocity circulating fluidized bed (CFB) has a unique internal circulation flow and remarkable advantages. Studies show that using a differential air supply in different beds accelerates the disturbance and mixing of materials in the bed. It also has superior advantages, including

* Corresponding author, jiachunxia_215@126.com

wide fuel adaptability, low pollution, and low wear, especially when burning inferior fuels and biomass.

Traditional computational particle fluid dynamics (CPFD) studies have focused on conventional CFB with uniform structures. The innovative high-low differential velocity CFB, featuring differentiated main bed and side beds, enables unique internal circulation and stratified combustion. This represents a shift from homogeneous fluidization to directional flow control, offering new solutions for efficient combustion of low-grade fuels. Compared with conventional CFB, high-low differential velocity CFB has a higher internal mixing efficiency and a more complex internal process. In actual working conditions, large solid particles cannot pass the high-speed bed and enter the low-speed bed. This phenomenon originates from the height difference between the main bed and the side bed, so small fuel particles enter the low-speed bed and combust, thereby reducing the erosion of the flag-shaped heated surface of the buried pipe [1]. Fuel first enters the main bed through side inlets, where its combustion generates a large amount of flue gas and heat. This heat raises the bed temperature and carries most of the small particles into the adjacent low-speed bed. The particles may pass to the working substance in the buried pipe, and finally return to the main bed for heat exchange, while the remaining part of the particles is taken away by the flue gas [2]. This internal circulation process prolongs the residence time of the material in the bed, thereby reducing heat loss and improving combustion and boiler efficiency.

The Barracuda engineering software package is a commercial package, which is developed based on the CPFD method [3]. Compared with the conventional computation fluid dynamics calculation software, this package is mainly focused on the particle phase and can restore the movement of particles in real time. Moreover, CPFD is developed based on the multiphase particle-in-cell (MP-PIC) method [4–6], and Eulerian and Lagrangian methods are used to solve governing equations in fluid and particle phases, respectively.

Abbasi et al. [7] used the CPFD method to study the effects of various operating parameters on the fluid dynamics of the gasifier feed section. The results show that the CPFD method can better predict the particle flow behavior of the gasifier feed section and the gas composition in the furnace. Loha et al. [8] conducted a three-dimensional numerical simulation of a bubbling fluidized bed biomass gasifier using the CPFD method. By adjusting the gasification temperature, equivalence ratio, and the ratio of steam to biomass, the pressure distribution and gas composition were obtained. The results are in good agreement with the experimental data. Ma et al. [9] numerically simulated the influence of different operating conditions on gas hydrodynamics in a high-density CFB using the CPFD method, and found that the number of vents on the riser does not have considerable effect on the solid flux, but does affect the hydrodynamic stability in the riser. Tu et al. [10] used the CPFD method to simulate a complex CFB with six cyclone separators using the Barracuda software to study the gas-solid flow characteristics in

a large-scale system. The results show that the dense region is clear in the bubble state of multiple explosions. Chen et al. [11] used the CPFD method to simulate the risers of the CFB, thus capturing the axial and radial non-uniform flow structure in the risers, revealing the characteristics of the core-annulus flow in the CFB. The calculation results also show that CPFD is more accurate than the two-fluid model with the same drag model, which shows a stronger predictive ability. Liu et al. [12, 13], based on the Barracuda platform, used the CPFD method to simulate the cold and hot states of the CFB test bench, and obtained the gas-solid velocity distribution and temperature distribution. By changing the primary air rate and the mixing ratio of semi-coke and straw, the internal flow and combustion characteristics of the riser were studied, and the ideal operating conditions were obtained.

Wang et al. [14] used the CPFD method to simulate the gas-solid flow in a CFB and analyzed the influence of key model parameters on CPFD simulation in detail. For example, the effects of particle close-packing volume fraction, mesh number, and particle size distribution on the flow in the whole CFB loop were found.

Shi et al. [15, 16] studied the influence of different particle size distributions (PSD) on particle back-mixing behavior during gas-solid flow using the CPFD method, and found that PSD has a significant effect on particle flow behavior in the lower region of the riser tubes, while the PSD effect in the upper region is negligible. Yan et al. [17] proposed a new method to calculate the distribution of coal feed based on the pressure drop and heat balance of a cyclone separator. A 600 MW supercritical CFB boiler was numerically simulated using Barracuda software combined with experimental data. The results show that the method can better predict the combustion characteristics as a boundary condition. It is concluded that the deviation of solid concentration below the furnace caused by the secondary air jet may be the cause of the uneven distribution of primary air velocity in the furnace. Shen et al. [18] analyzed the gas-solid flow and the change of residual coke in a 350 MW CFB boiler under variable working conditions. The study found that, in the load-rising stage, the average value of residual coke in the furnace was significantly higher than that in the boiler start-up stage. In the load-drop stage, the average value of coke was lower than that in the load-rising stage. The combustion rate of residual coke does not match the coal feeding rate under variable load conditions.

The performed literature survey on CFB indicates that most CPFD simulations are focused on conventional CFB, and research on high-low differential velocity CFB boilers is scarce. Moreover, most research on CFB boilers is conducted using Ansys Fluent software. To this end, the CPFD method is applied to simulate the three-dimensional steady-state combustion of a high-low differential velocity CFB boiler. This study fills the gap in research on the combustion characteristics of oil shale fuel in both high- and low-temperature CFB boilers based on the CPFD model.

Unlike conventional CPFD–CFB models for homogeneous structures, this study develops a specialized model for a high-low differential velocity

CFB that reveals their unique particle back-mixing and internal circulation patterns. By coupling asymmetric flow fields with combustion reactions, the model demonstrates how this back-mixing enhances combustion efficiency while reducing pollutants, offering a new methodology and theoretical basis for optimizing such specialized CFB systems. The main contributions of this paper can be summarized as follows:

(1) Fuel combustion in the boiler under different excess air coefficients is analyzed, and the results are compared with those under actual working conditions. The distributions of temperature and gas composition, variations in chemical reactions, and the distribution of particle residence time are obtained, and the excess air coefficient is optimized. This article can provide a reference for studying fluidized bed boilers.

(2) Gas emissions of the boiler under different excess air coefficients are analyzed numerically. Furthermore, the influence of different air volume ratios of the main bed and side beds on the emission of NOx and other pollutant gases is explored. The obtained results are then analyzed under different working conditions to determine the optimal operating conditions.

2. Numerical simulation

2.1. Governing equations

Ignoring interphase mass transfer, the continuity equation for the gas phase can be expressed as follows:

$$\frac{\partial \theta_g \rho_g}{\partial t} + \nabla\left(\theta_g \rho_g u_g\right) = 0, \tag{1}$$

where ρ_g, u_g, and θ_g are the density, velocity, and volume fraction of the gas phase, respectively.

The momentum conservation equation for the gas phase is as follows:

$$\frac{\partial \theta_g u_g}{\partial t} + \nabla\left(\theta_g u_g u_g\right) = -\frac{1}{\rho_g}\nabla P - \frac{1}{\rho_g} F + \theta_g g + \frac{1}{\rho_g}\nabla \tau, \tag{2}$$

where P and F are the pressure and macroscopic stress tensor of the gas phase, respectively, and τ is the unit volume momentum exchange rate between the gas phase and the particle phase.

The stress tensor F can be calculated using the following expression:

$$F = \iiint f V_p \rho_p \left[D\left(u_g - u_p\right) - \frac{1}{\rho_p}\nabla P \right] dV_p d\rho du_p . \tag{3}$$

The momentum equation of the particle phase is as follows:

$$\frac{du_p}{dt} = D\left(u_g - u_p\right) - \frac{1}{\rho_p}\nabla P + g - \frac{1}{\theta_p \rho_g}\nabla \tau_p, \tag{4}$$

where u_p, ρ_p, and τ_p denote the velocity, density, and normal stress of the particle phase, respectively.

Equations (1–4) show the generated acceleration originating from the combined action of aerodynamic drag, pressure gradient, gravity, and normal stress gradient between particles. In each grid, the volume fraction of particles is as follows:

$$\theta_p = \iiint f V_p d\rho_p du_p. \tag{5}$$

In the present study, the interparticle collision is calculated using the normal stress model:

$$\tau = \frac{P_s \theta_p^{\beta}}{\max\left[\left(\theta_{cp} - \theta_p\right), \varepsilon\left(1 - \theta_p\right)\right]}, \tag{6}$$

where P_s is the material parameter, $2 < \beta < 5$ is the model parameter [19], θ_{cp} is the volume fraction of particle dense packing and ε is a quantity constructed to eliminate singular points in the model [20].

2.2. Calculation of particle properties

In the Barracuda software, it is assumed that particles are spherical, and the particle radius is calculated using the following expression:

$$r_{\text{particle}} = \left(\frac{3}{4\pi} V_{\text{particle}}\right)^{1/3}. \tag{7}$$

Due to the combustion of pulverized coal pyrolysis and volatile fraction, the particle density may change. Consequently, the following method is used in the calculations:

$$m_{\text{particle}} = \sum_i m_{\text{volatile},i} + \sum_i m_{\text{volatile},i}, \tag{8}$$

$$V_{\text{particle}} = \sum_i v_{\text{solid},i} + \sum_i v_{\text{volatile},i}, \tag{9}$$

where $m_{\text{volatile},i}$ and $v_{\text{volatile},i}$ are the mass and volume of the i-th volatile fraction, respectively. Moreover, $m_{\text{solid},i}$ and $v_{\text{solid},i}$ are the mass and volume of the i-th particle, respectively.

The particle density is defined as follows:

$$\rho_{\text{particle}} = \frac{m_{\text{particle}}}{V_{\text{particle}}}, \tag{10}$$

$$v_{\text{solid},\,i} = \frac{m_{\text{solid},i}}{\rho_{\text{solid},i}}. \tag{11}$$

It should be indicated that, during the volatilization process, the fuel releases a large amount of gas after heating. Based on the Arrhenius equation, the reaction rate can be expressed as follows:

$$k = c0T^{C1}P^{C2}\rho_f^{c3}\exp(-E/T + E_0), \tag{12}$$

where T is the temperature, P denotes the pressure, ρ_f is the fluid density, and E is the activation energy.

Meanwhile, the volatile fraction release rate can be calculated as follows:

$$\frac{\mathrm{d}m_{\text{volatile}}}{\mathrm{d}t} = -km_{\text{volatiles}}. \tag{13}$$

2.3. Drag model

The trapping forces of the fluid and particle phases are defined as follows:

$$D_{\text{s}} = C_{\text{d}}\frac{3}{8}\frac{\rho_g}{\rho_s}\frac{|u_{\text{f}} - u_{\text{s}}|}{r_{\text{s}}}, \tag{14}$$

where u_{f} and u_{s} are the velocity vectors of the fluid and particle phases, respectively, and D_{s} is the traction function.

In the Barracuda software, drag models include the WenYu model, the Ergun model, the WenYu–Ergun model, and the EMMS model. The EMMS model employs a non-uniform drag model, simplifying the actual complex particle clusters into sparse, regular spherical particle clusters. It is more suitable for Geldart Class A particles, achieving higher simulation accuracy for this particle type. However, the particle size distribution in CFB boilers more closely resembles that of Geldart Class B particles, making it difficult to form agglomerates similar to those of Geldart Class A particles. This may lead to reduced model accuracy, rendering the EMMS model unsuitable for CFB boiler simulations.

The WenYu–Ergun model combines the strengths of both the WenYu and Ergun models, offering excellent simulation accuracy for particles of varying sizes. It effectively simulates the distribution between the dense-phase and dilute-phase zones in CFB boilers. Therefore, the WenYu–Ergun gas–solid drag model is used for the calculations. This drag model can accurately predict the flow characteristics within the CFB 14.

The WenYu–Ergun drag model is expressed as follows:

$$\theta_p > 0.85\theta_{cp} \qquad D = D_p^2, \tag{15}$$

$$\theta_p < 0.75\theta_{cp} \qquad D = D_p^1, \tag{16}$$

$$0.85\theta_{cp} \geq \theta_p \geq 0.75\theta_{cp} \quad D = \frac{\theta_p - 0.85\theta_{cp}}{0.85\theta_{cp} - 0.75\theta_{cp}}\left(D_p^2 - D_p^1\right) + D_p^1, \tag{17}$$

where D_p^1 and D_p^2 are the coefficients of the WenYu and Ergun models, respectively.

2.4. Simulation of chemical reaction

Take the following chemical reaction as an example:

$$C(s) + H_2O \rightarrow CO + H_2, \tag{18}$$

$$R = 219\frac{m^3}{kg \bullet K \bullet s} T \exp(-\frac{22645\text{K}}{\text{T}})\rho_c[H_2O], \tag{19}$$

where T is the temperature, ρ_c is the density of carbon particles, and $[H_2O]$ denotes the volume concentration of H_2O.

The concentration changes of reactants and products in these reactions can be calculated by solving the following differential equations:

$$k_0 = 219\frac{m^3}{kg \bullet K \bullet s} T \exp(-\frac{22645K}{T})\rho_c, \tag{20}$$

$$\frac{d[C(s)]}{dt} = -219\frac{m^3}{kg \bullet K \bullet s} T \exp(-\frac{22645\text{K}}{\text{T}})\rho_c[H_2O], \tag{21}$$

$$\frac{d[H_2O]}{dt} = \frac{d[C(s)]}{dt} \qquad \frac{d[CO]}{dt} = -\frac{d[C(s)]}{dt}, \tag{22}$$

$$\frac{d[H_2]}{dt} = -\frac{d[C(s)]}{dt}. \tag{23}$$

The chemical reaction rate is as follows:

$$r = k_0[H_2O]. \tag{24}$$

The chemical reaction rate constant is the following:

$$k_0 = 219\frac{m^3}{kg \bullet K \bullet s} T \exp(-\frac{22645K}{T})\rho_c. \tag{25}$$

The equivalent chemical equation is as follows:

$$C(s) + H_2O \rightarrow CO + H_2. \tag{26}$$

2.5. Calculation of wall radiation heat transfer

In the Barracuda software, only the radiative heat transfer between the wall and the particles near the wall is considered in calculations, while the radiative heat transfer between particles and the radiative heat transfer between the fluid and the wall are ignored. This can be expressed as follows:

$$q_{\mathrm{wp}} = A_{\mathrm{w}} F_{\mathrm{wp}} \varepsilon_{\mathrm{wp}} \sigma (T_{\mathrm{w}}^4 - T_{\mathrm{p}}^4) \ , \tag{27}$$

where A_{w} is the wall area, T_{w} is the wall temperature, T_{p} denotes the average particle temperature within a calculation cell, F_{wp} is the calculated view factor, σ is the Boltzmann constant, and $\varepsilon_{\mathrm{wp}}$ is the effective emissivity between wall and particle.

The expression for $\varepsilon_{\mathrm{wp}}$ is as follows:

$$\varepsilon_{\mathrm{wp}} = (\frac{1}{\varepsilon_{\mathrm{p}}} + \frac{1}{\varepsilon_{\mathrm{w}}} - 1)^{-1} \ , \tag{28}$$

where ε_{w} is the wall emissivity and ε_{p} denotes the volume-weighted average particle emissivity.

2.6. Calculation of convective heat transfer

The convective heat transfer coefficient between the wall and the fluid, the heat transfer coefficient in the dense-phase region, and the heat transfer coefficient between the fluid and the particles are calculated using the following equations.

The convective heat transfer coefficient between the fluid and the wall is as follows:

$$h = (1 - f_d) h_1 + f_d h_d \ , \tag{29}$$

where h_1 and h_d are the heat transfer coefficients of the dilute phase and the particle phase, respectively, f_d is the time-averaged proportion of the wall surface covered by the particle phase, k_f is the thermal conductivity of the fluid, L is the length of a single grid, and μ_f is the fluid viscosity.

The above-mentioned parameters can be determined using dimensionless numbers [21]:

$$\frac{h_1 L}{k_f} = Nu_1 = 0.546 \mathrm{Re}_1 + 3.66 \ , \tag{30}$$

$$\mathrm{Re}_1 = \frac{\rho_g u_g L}{\mu_f} . \tag{31}$$

The convective heat transfer coefficient in the dense phase is given by the following:

$$\frac{h_d d_p}{k_f} = Nu_d = 0.525 \mathrm{Re}_1^{0.75} , \tag{32}$$

$$f_d = 1 - e^{-10 \frac{\theta_p}{\theta_{cp}}} . \tag{33}$$

The convective heat transfer coefficient between the particles and the gas is given as follows [22]:

$$\frac{h_p d_p}{k_f} = Nu_p = 0.37\,\mathrm{Re}_p^{0.6} + 0.1, \tag{34}$$

$$\mathrm{Re}_p = \frac{\rho_g u_g d_p}{\mu_f}. \tag{35}$$

3. Boiler structure, initial conditions, and boundary conditions

In the present study, a 65-t/h high-low differential velocity CFB is considered as the research object. The simulation model is shown in Figure 1.

The model mainly consists of a boiler chamber, two feed ports, 16 secondary air nozzles, and a water wall. It uses primary and secondary air flows to supply high- and low-speed beds, respectively. Furthermore, it consumes Maoming oil shale as fuel. The results of the proximate and ultimate analyses of the fuel are shown in Table 1.

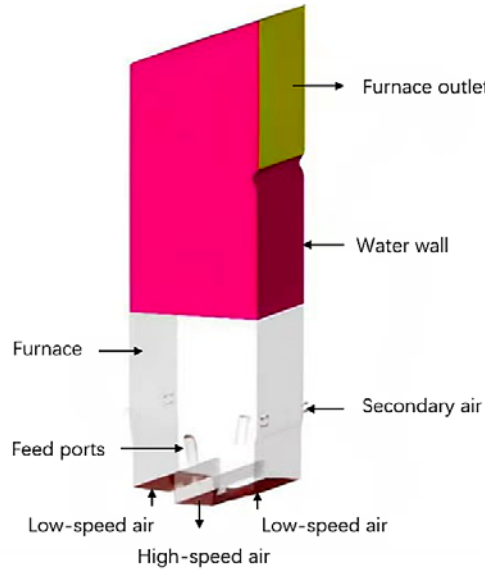

Fig. 1. Schematic diagram of the computational model.

Table 1. Proximate and ultimate analyses of Maoming oil shale

Proximate analysis, %				Low heat value, MJ/kg	Ultimate analysis, %				
M_{ar}	V_{ar}	A_{ar}	FC_{ar}	$Q_{net,ar}$	C_{ar}	H_{ar}	O_{ar}	N_{ar}	S_{ar}
18.10	16.51	62.99	2.40	4.1	9.70	1.65	6.12	1.08	0.36

Abbreviations: M_{ar} – moisture, as-received basis; V_{ar} – volatile matter, as-received basis; A_{ar} – ash content, as-received basis; FC_{ar} – fixed carbon, as-received basis; $Q_{net,ar}$ – net calorific value, as-received basis; C_{ar} – carbon, as-received basis; H_{ar} – hydrogen content, as-received basis; O_{ar} – oxygen content, as-received basis; N_{ar} – nitrogen content, as-received basis; S_{ar} – sulfur content, as-received basis.

The particle size distribution is shown in Figure 2. The bed material is shale ash with a height of 400 mm. In the initial phase, the material accumulates at the bottom of the furnace. The oil shale enters the high-speed bed through both sides of the furnace, while the airflow enters the furnace from the bottom of the bed. The bed material begins to fluidize, and the bed material is continuously discharged from the outlet simultaneously. Finally, the furnace reaches steady-state conditions. Figure 3 shows the variations of the gas mass fraction at the furnace outlet. It is observed that fluctuations of the gas mass fraction at the outlet are small after 25 seconds. Accordingly, the results are averaged over the time period of 25–45 s. The time-averaged values of the corresponding physical quantities are used to analyze the results.

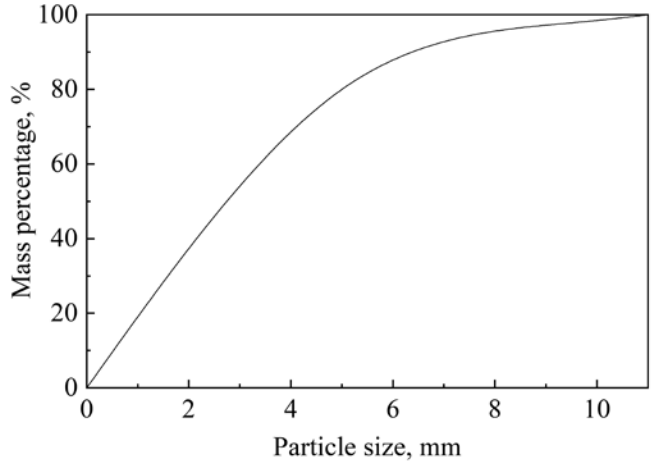

Fig. 2. Particle size distribution of Maoming oil shale.

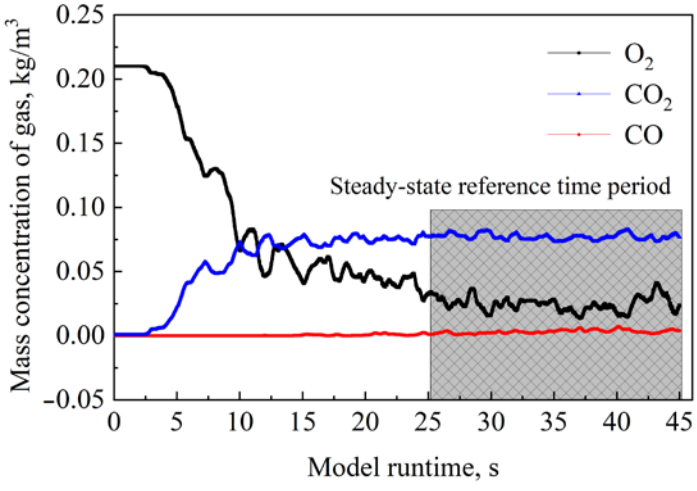

Fig. 3. Outlet gas mass concentration vs time.

The simulated operating conditions are shown in Table 2. The chemical reactions and rate equations are presented in Table 3 [23–27].

Table 2. Simulation conditions

Case	Excess air coefficient a	Feed quantity, kg/h
1	1.10	39265
2	1.15	39265
3	1.20	39265

Table 3. Chemical reaction equations and reaction rates

Reaction equations	Reaction rate, $mol \cdot m^{-3} \cdot s^{-1}$
Heterogeneous reaction	
$C(s) + H_2O \rightarrow CO + H_2$	$r_1 = 1.272 m_s T \exp(-22645/T)[H_2O]$
$C + CO_2 \rightarrow 2CO$	$r_2 = 1.272 T \exp(-22645/T)[CO_2]$
$2C(s) + O_2 \rightarrow 2CO$	$r_3 = 1.47 \times 10^5 \theta_p T \exp(-13590/T)[O_2]$
$CO + H_2 \rightarrow C(s) + H_2O$	$r_4 = 1.04 \times 10^{-4} m_s T^2 \exp(-6319/T - 17.29)[CO][H_2]$
$2CO \rightarrow CO_2 + C(s)$	$r_5 = 1.04 \times 10^{-4} m_s T^2 \exp(-2363/T - 20.92)[CO]$
Homogeneous gas phase reaction	
$CO + 0.5O_2 \rightarrow CO_2$	$r_6 = 5.62 \times 10^{12} \exp(-16000/T)[CO][O_2]$
$CO + H_2O \rightarrow CO_2 + H_2$	$r_7 = 7.68 \times 10^{10} \exp(-36640/T)[H_2O][CO]$
$CH_4 + O_2 \rightarrow CO_2 + 2H_2$	$r_8 = 3.552 \times 10^{11} T^{-1} \exp(-15700/T)[CH_4][O_2]$
Reaction of nitrides with sulfides	
$H_2S + 1.5O_2 \rightarrow SO_2 + H_2O$	$r_1 = 5.2 \times 10^8 \exp(-2321/T)[H_2S][O_2]$
$NH_3 + 1.25O_2 \rightarrow NO + 1.5H_2O$	$r_2 = 3.1 \times 10^8 \exp(-25000/T)[NH_3][O_2]$
$NO + CO \rightarrow 0.5N_2 + CO_2$	$r_3 = K_3 \dfrac{K_{3a}[NO](K_{3b}[CO] + K_{3C})}{K_{3a}[NO] + K_{3b}[CO] + K_{3C}}$ $K_3 = 1.952 \times 10^7 \exp(-25000/T)$ $K_{3a} = 18.26\ K_{3b} = 7.86\ K_{3c} = 0.002531$
$HCN + 0.75O_2 \rightarrow CNO + 0.5H_2O$	$r_4 = 2.14 \times 10^8 \exp(-10000/T)[HCN][O_2]$

Continued on the next page

Table 3. *Continued*

Reaction equations	Reaction rate, mol·m^{-3}·s^{-1}
CNO + 0.5O_2 → NO + CO	$r_5 = K_5 \frac{K_{5a}}{K_{5a} + K_{5b}[NO]}[HCN][O_2]$ $K_5 = 2.14 \times 10^8 \exp(-10000/T)$ $K_{5a}/K_{5b} = 1.02 \times 10^{12} \exp(-25499/T)$
CNO + NO → N_2O + CO	$r_6 = K_6[HCN][O_2]\frac{K_{6a}[NO]}{K_{6a} + K_{6b}[NO]}$ $K_{6a}/K_{6b} = 1.02 \times 10^{12} \exp(-25499/T)$
N_2O + CO → N_2 + CO_2	$r_7 = 1.24 \times 10^9 \exp(-5913/T)[N_2O][CO]$
N_2O + 0.5O_2 → N_2+O_2	$r_8 = 1.5 \times 10^{11} \exp(-20159/T)[N_2O][O_2]$
NH_3 + 0.75O_2 → 0.5N_2 + 1.5H_2O	$r_9 = 4.96 \times 10^8 \exp(-10000/T)[NH3][O_2]$
2NH_3 + 3NO → 2.5N_2 + 3H_2O	$r_{10} = 1.1 \times 10^{12} \exp(-27676/T)[NH3]^{0.5}[O_2]^{0.5}[NO]^{0.5}$
N_2O + C → N_2 + CO	$r_{11} = 2.9 \times 10^9 \exp(-1711/T)[N_2O]$
NO + C → 0.5N_2 + CO	$r_{12} = 5.85 \times 10^7 \exp(-12000/T)[NO]$
NO + 0.5C → 0.5N_2 + 0.5C_O2	$r_{13} = 1.3 \times 10^5 \exp(-1712/T)[NO]$

The performance of the developed model can be evaluated by comparing the numerical results of Case 2 with the field test data. A grid-independent test is conducted based on three mesh sizes, and the comparison between the calculated T_{ll}, T_{rl}, and T_h (T_{ll} denotes left low-speed bed, T_{rl} denotes right low-speed bed, T_h denotes high-speed bed) and the measured values are shown in Table 4.

Table 4. Comparison of simulated and experimental temperatures for different grids

Grid category	Mesh number	Simulated value T_{ll}	Test value T_{ll}	Simulated value T_h	Test value T_h	Simulated value T_{rl}	Test value T_{rl}	Average error
Coarse	67452	687 °C	760 °C	689 °C	747 °C	679 °C	761 °C	9.3%
Medium	85932	707 °C	760 °C	711 °C	747 °C	695 °C	761 °C	8.2%
Fine	95172	716 °C	760 °C	718 °C	747 °C	698 °C	761 °C	5.9%

On-site test data exhibit a certain degree of measurement uncertainty. The uncertainty in thermocouple temperature measurements primarily stems from the thermocouple's inherent accuracy (±2.5 °C), radiation errors, and temperature fluctuations within the furnace. The combined uncertainty is estimated to be approximately ±15 °C. However, the overall error remains within the specifications outlined in the test procedures.

Table 4 presents the comparison between simulated temperatures and measured values under three mesh configurations. As the number of mesh cells increased from 67452 to 95172, the simulated main bed temperature (T_{ll}) rose from 687 °C to 716 °C, while the deviation from the measured value (760 °C) decreased from 9.6% to 5.8%. This indicates that the simulation results exhibit sensitivity to grid resolution, particularly when capturing complex gas–solid flow in the dense-phase zone at the bottom. The ultimately selected medium grid scheme (85932) significantly conserves computational resources while maintaining accuracy, with an average error of 8.2%, within an engineering-acceptable range.

4. Results and discussion

4.1. Combustion characteristics

4.1.1. Temperature distribution

Figures 4 and 5 show the time-averaged temperature distribution of gas and particles with an excess air coefficient of 1.15. It is observed that the fluid temperature near the feed ports in the dense-phase zone of the furnace

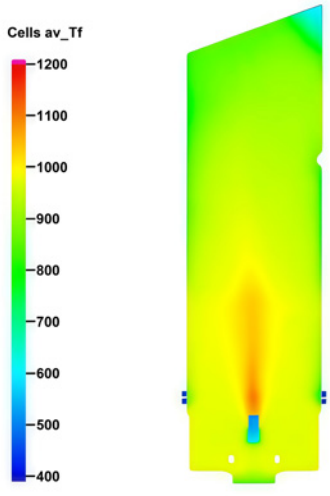

Fig. 4. Time-averaged temperature distribution of the combustion gas (showing higher temperatures near the feed ports in the dense-phase zone).

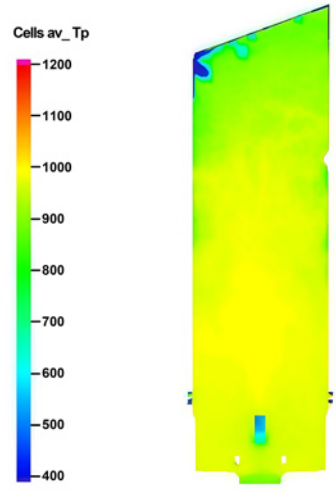

Fig. 5. Time-averaged temperature distribution of particles (illustrating lower temperatures than the surrounding gas near the feed ports).

is higher than the particle temperature, with the maximum temperature difference reaching 100 °C. In the dilute-phase region, the fluid temperature and particle temperature are relatively uniform, with a temperature difference of approximately 20 °C. This is because the oil shale contains fewer volatile components, so combustion occurs in the gas phase. Due to the lower specific heat capacity of gas, its temperature increases faster. In this regard, Table 4 indicates that the calculated furnace temperature is lower than the actual operating temperature. Meanwhile, the measured temperature from thermocouples has some uncertainties. The calculation error is within the allowable range, so the model is verified to predict temperatures with reasonable accuracy.

4.1.2. Chemical reaction rate

In order to simplify the calculations, a simplified model is used to simulate the chemical reactions. Figure 6(a)–(i) shows the reaction rates of different simplified models in the fluidized bed furnace with an excess air coefficient of 1.15. It is found that all heterogeneous reaction rates in the reactor at a height of 4 m, at the bottom of the bed, and at the oil shale inlet approach 0. The C–O_2 combustion provides heat for gasification, so the rates of the gasification reactions C–H_2O and C–CO_2 are relatively large. For the homogeneous reaction rate, the combustion reactions of CO and CH_4 are the most stable in the whole furnace, and these reactions mainly occur at heights near the feed ports.

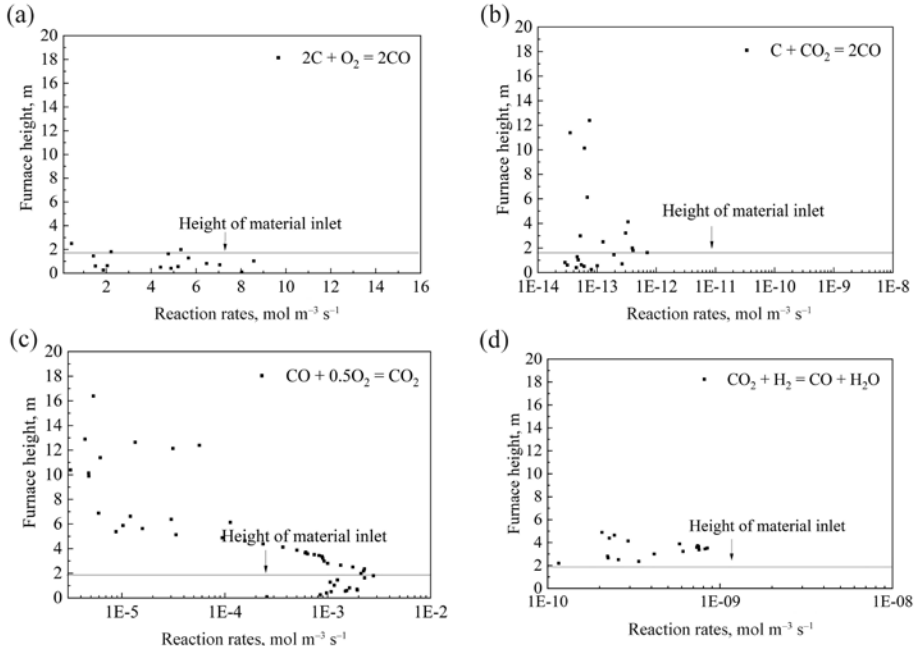

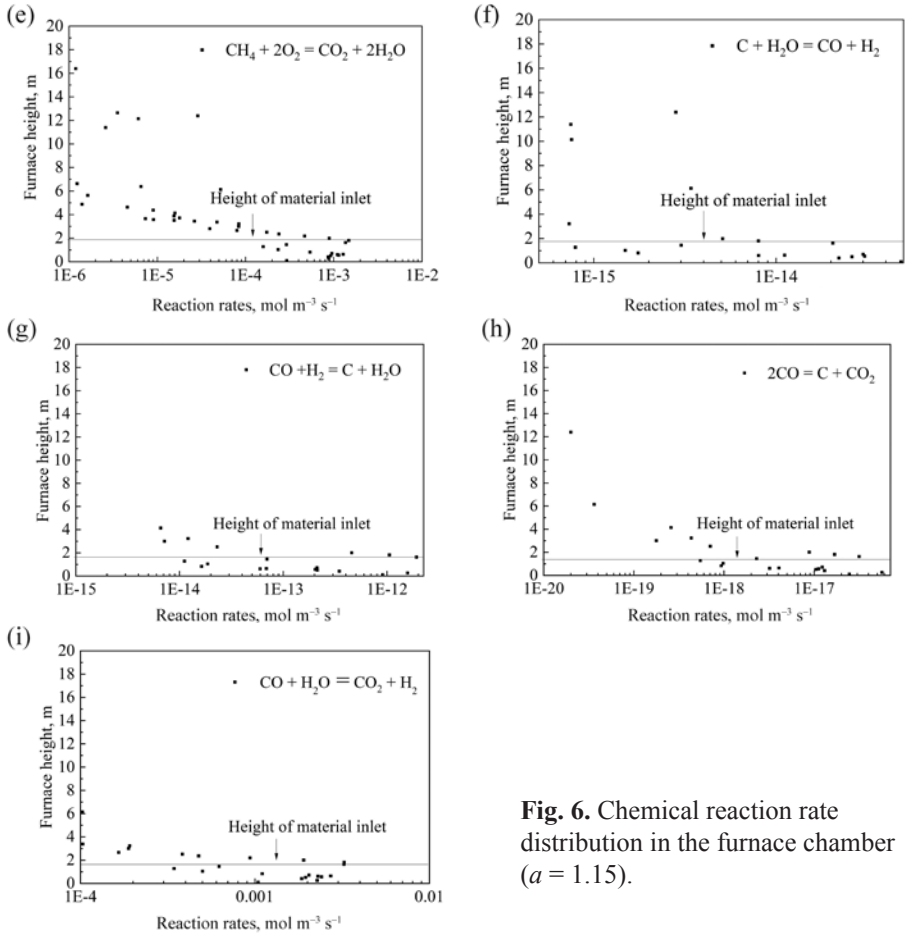

Fig. 6. Chemical reaction rate distribution in the furnace chamber (a = 1.15).

4.1.3. Particle residence time

In order to obtain the degree of particle back-mixing, the residence time distribution (RTD) density function E(t) of particles in the furnace under different excess air ratios is shown in Figure 7. It is observed that the distribution has a spike and also exhibits a certain trailing phenomenon, which indicates that the particles are close to plug flow. However, due to the exchange between particles, the average residence time is larger than that of plug flow. Considering the strong downward flow of particles at the bed wall, the residence time distribution has a late peak and pronounced trailing [16].

When a is small (1.10), the primary air volume is relatively low, resulting in a lower gas velocity in the dense-phase zone at the bed bottom. This makes it more difficult to lift large particles, facilitating the formation of intense

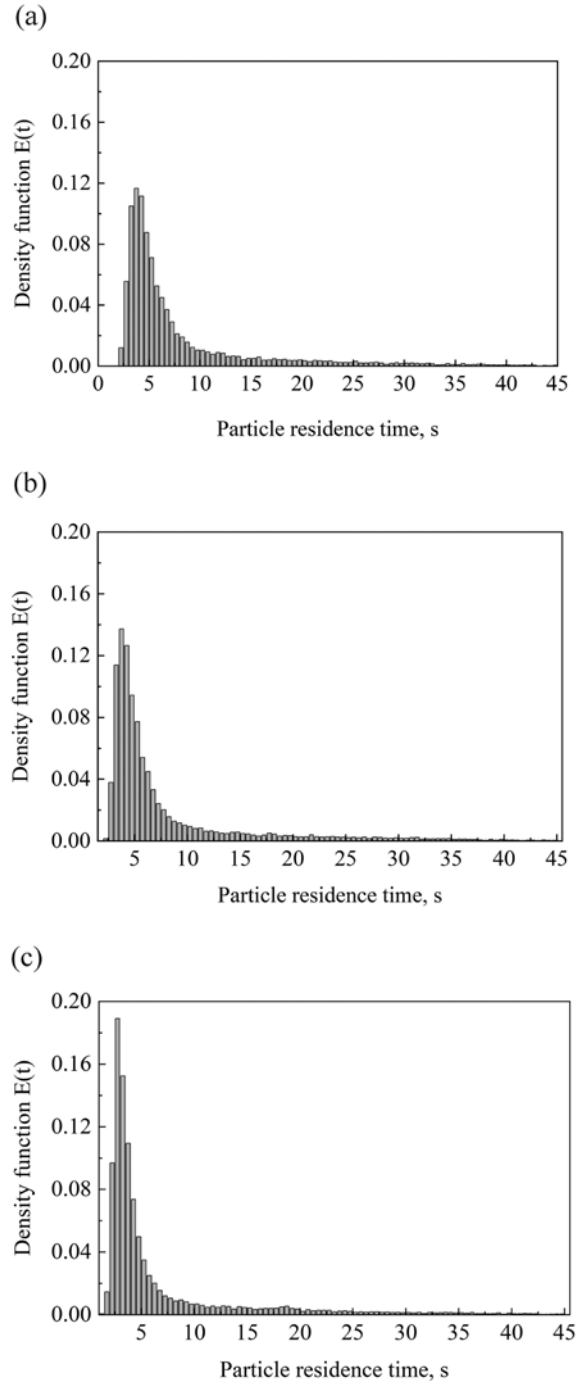

Fig. 7. Particle residence time distribution under different excess air ratios: a = 1.10 (a); a = 1.15 (b); a = 1.20 (c).

vortices and recirculation at the bottom, which leads to more severe back-mixing. When *a* is large (1.20), the primary air volume increases, raising the overall gas velocity. The enhanced penetration of the gas flow allows more particles to be directly entrained upward, reducing the opportunity for particles to linger and circulate at the bottom. Consequently, the degree of back-mixing is mitigated.

Figure 8 illustrates the spatial distribution of particle residence time. It is challenging to compare the spatial distribution of particle residence times based solely on figures. For example, particles in the dense-phase zone of the bed have a higher residence time, while particles in the dilute-phase zone have a lower residence time. This is mainly because the large particles in the dense-phase zone require more time to transition to the dilute-phase zone. Particles with smaller sizes in the dilute-phase zone leave the furnace quickly, and the residence time of particles just entering the fuel inlet is relatively short.

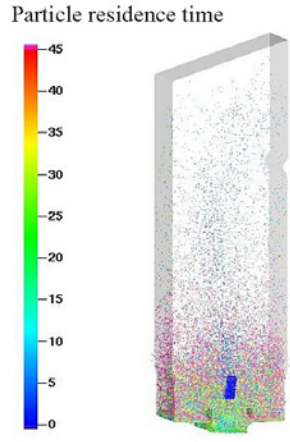

Fig. 8. Spatial distribution of particle residence time (a = 1.15).

Figure 9 show the cumulative distribution function F(t) curves of particle residence time under different excess air ratios. It is worth noting that the ideal plug-flow F(t) curve is a vertical line, and the smaller the slope of the F(t) curve, the higher the degree of back-mixing [28]. The results indicate that when a = 1.10, the back-mixing behavior is more intense and more favorable for combustion. Therefore, it is recommended to use 10% excess air in engineering processes.

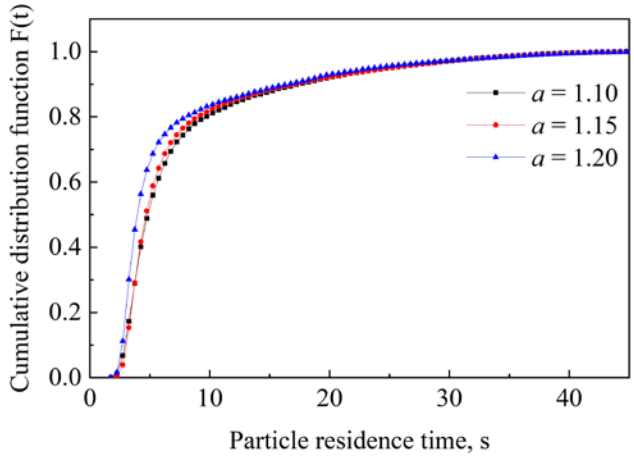

Fig. 9. Cumulative distribution of particle residence time.

4.1.4. Gas distribution

Figure 10 shows the concentration distribution of O_2 and CO_2 in the furnace at different excess air ratios after the model has run for 45 s. Inside the furnace, a small portion of CO_2 gas originates from the primary and secondary air, while the main part is produced by combustion. In the dense zone at the bottom of the furnace, a large number of oil shale particles burn, which results in areas with low O_2 concentrations and relatively high CO_2 concentrations. Although the injection of secondary air in the dilute-phase zone increases the O_2 concentration along the furnace height, its weak diffusion results in poor mixing efficiency, consequently forming a low-temperature zone near the air inlet.

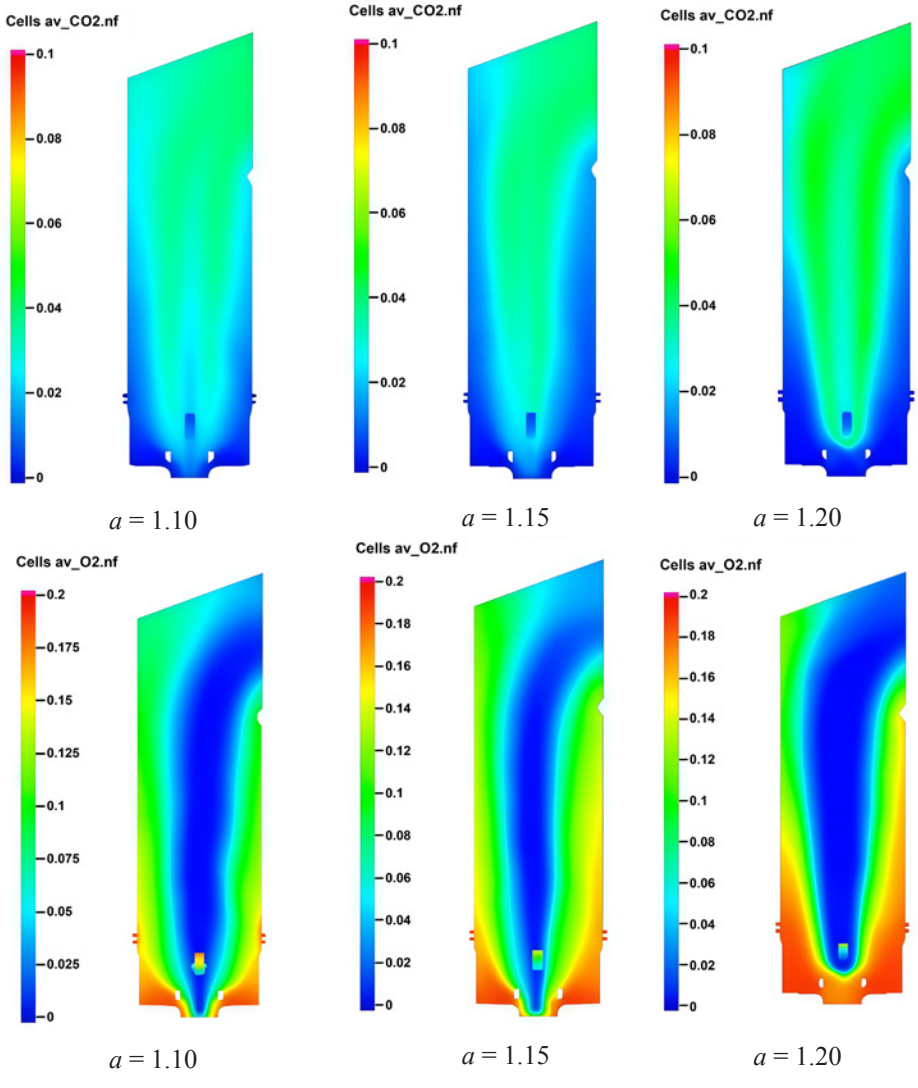

$a = 1.10$ $a = 1.15$ $a = 1.20$

$a = 1.10$ $a = 1.15$ $a = 1.20$

Fig. 10. Distribution of O_2 and CO_2 concentrations under different excess air ratios.

Table 5 shows the mass fraction of the gas composition at the outlet. The test values were obtained using a flue gas analyzer at the center of the boiler outlet pipe under stable operating conditions at the boiler's rated load (65 t/h) and an excess air coefficient of 1.15. During the measurement period, the feed rate was maintained at 39265 kg/h. It is observed that the concentrations of O_2 and CO_2 at the outlet are lower than the experimental values. Figure 3 indicates that there is an intermediate product, CO, in the flue gas at the outlet, demonstrating that the oil shale in the furnace is not fully burned, so the CO_2 concentration is 27% lower than the measured value.

The decrease in the O_2 concentration at the outlet is affected by the secondary airflow. Figure 10 confirms that the oxygen content in the center of the furnace is relatively low. This is due to the insufficient diffusion of the secondary airflow, which makes the oxygen inside the furnace anoxic. This phenomenon not only leads to insufficient combustion in the furnace and decreases the CO_2 concentration, but also reduces the O_2 concentration at the outlet and leads to a deviation between the calculated concentrations and the measured values. It is worth noting that the deviation between the two gases is less than 25%. It is concluded that the calculated results are in good agreement with the experiment, and the developed model can be used to simulate the combustion in CFB boilers.

Table 5. Mass fraction of main gas components at the outlet, %

Gas	Numerical calculation result	Test value	Deviation
O_2	2.9	3.7	21
CO_2	7.8	10.8	27

4.2. Simulation of pollutant gases

4.2.1. Effects of different excess air ratios on the emission of pollutant gases

Figure 11 shows the molar fraction of the pollutant gases (CO_2, CO, NO, and SO_2) at the outlet of the high-low differential velocity CFB with an excess air ratio of 1.15. It is observed that the deviation between the calculated values and the experimental results is within a reasonable range, which reflects the accuracy of the model.

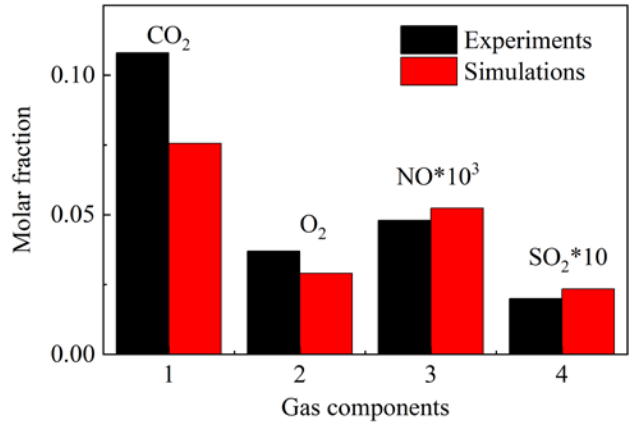

Fig. 11. Molar fraction of gases at the outlet (a = 1.15).

Figures 12 and 13 show the time-averaged distribution of NO and N_2O concentrations along the furnace height, respectively. In the bottom region, the formation of NO gas mainly originates from coke combustion. Near the feed opening, coke combustion and volatile fraction release rapidly increase the concentration of NO until a peak is reached above the feed opening, where the generation and reduction reactions reach equilibrium. NO then reacts with CO or coke, and N_2 is produced. Therefore, the NO concentration decreases along the height of the furnace. More specifically, NO concentration decreases to 52 ppm at the outlet.

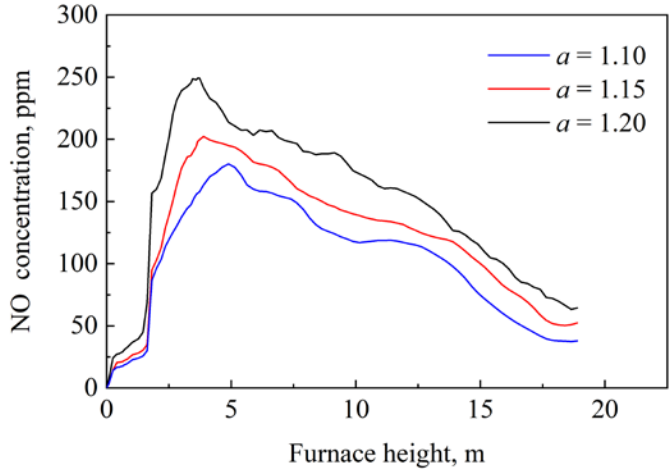

Fig. 12. Time-average distribution of NO gas concentration along the height of the furnace chamber.

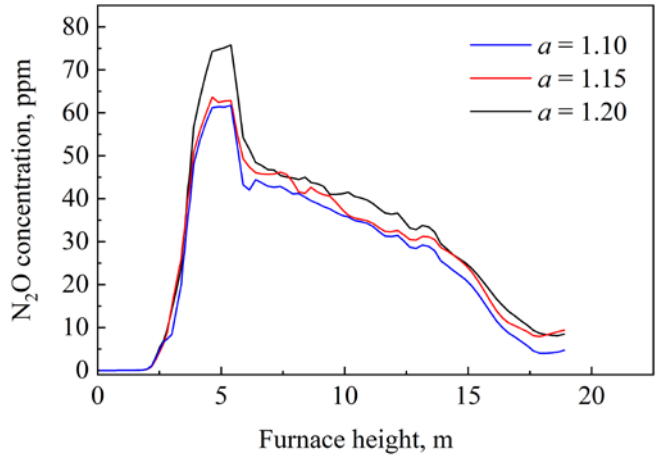

Fig. 13. Time-averaged distribution of N_2O gas concentration along the height of the furnace chamber.

N_2O is mainly derived from the reaction between NO and CNO, and its concentration increases with increasing NO concentration. At a certain position above the feed opening, N_2O production is balanced by the reduction reaction. At this point, the N_2O concentration reaches its maximum and then decreases along the furnace height.

As the excess air ratio increases, NO concentration also increases gradually, which is mainly due to the reaction between HCN and NH_3. Consequently, the simultaneous decrease in char and CO weakens the reduction of NO, leading to higher NO concentrations [29].

Figure 14 illustrates the time-averaged distribution contour of the combustion gas. In the vicinity of the feed port, the NO concentration reaches its

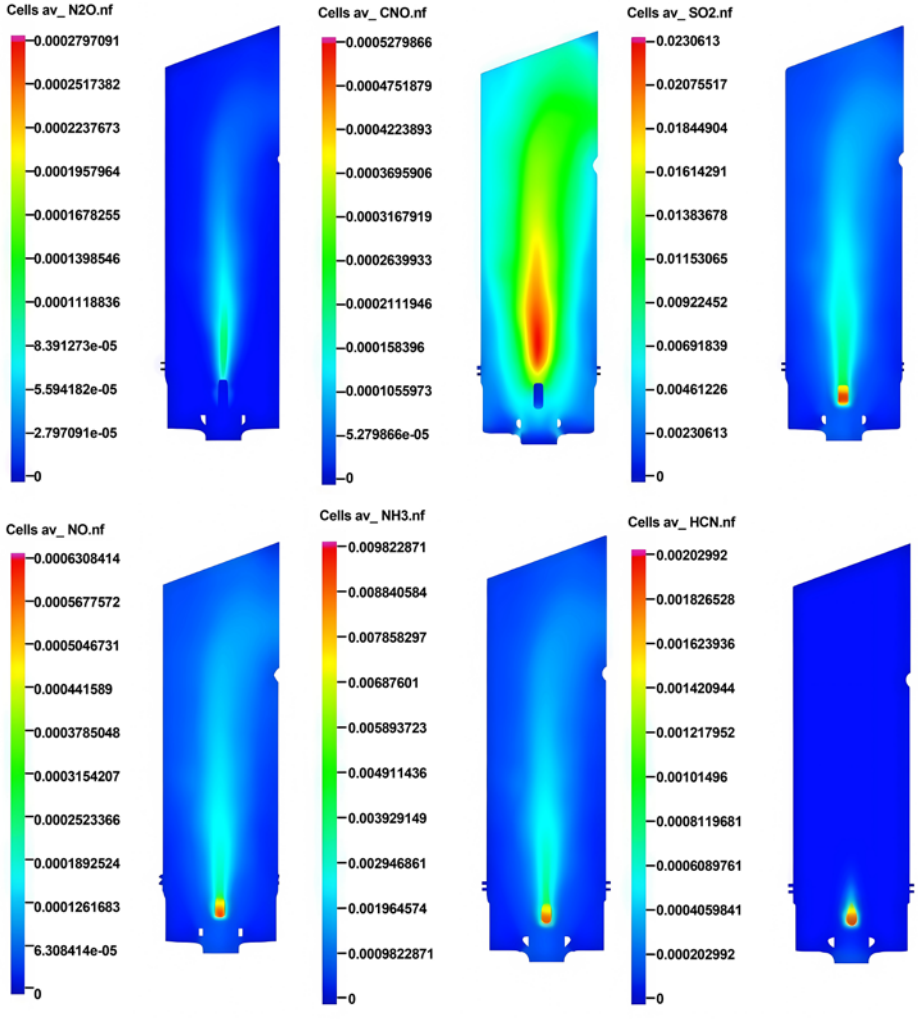

Fig. 14. Contours of the time-averaged distribution of gas components (a = 1.15).

maximum, indicating the oxidation of nitrogen. During the pyrolysis process, NH_3 is released into the furnace, and HCN is quickly converted to CNO, most of which is produced near the feed port. Moreover, N_2O is mainly produced from the reaction between CNO and NO. Consequently, the N_2O concentration is relatively high above the feed port.

As shown in Figures 12 and 14, the NO concentration peaks near the feed inlet, primarily originating from two competing pathways: rapid oxidation of fuel nitrogen (mainly present as HCN and NH_3 in volatile matter) in the high-temperature zone, and oxidation of carbon nitrogen. However, the unique flow structure of the high-low differential velocity CFB plays a crucial role. Intense particle recirculation creates localized zones rich in coke and CO within the furnace, establishing ideal conditions for both heterogeneous reduction (e.g., $NO + C \rightarrow 0.5N_2 + CO$) and homogeneous reduction (e.g., $NO + CO \rightarrow 0.5N_2 + CO_2$) of NO. Consequently, along the furnace height, the NO concentration exhibits a decreasing trend after reaching its peak.

4.2.2. Effect of different air distribution volumes in the main bed and side beds on the emission characteristics of pollutant gases

The CFB staged combustion technology can achieve low emissions of nitrogen and sulfur oxides to a certain extent. In a 65-t/h high-low differential velocity CFB, the fuel is supplied to the main bed from both sides of the furnace, and the airflow enters the main bed and side beds, respectively. This segmented air supply reduces NOx and other gas emissions. Figure 15 shows the NO and SO_2 emissions at the furnace outlet under different air volume ratios of the main bed and side beds with an excess air ratio of 1.10. It is observed that the lowest pollution can be achieved when the air volume ratio of the main bed and side beds is 1.5:1. This is the optimal operating condition to minimize pollution emissions in actual operation.

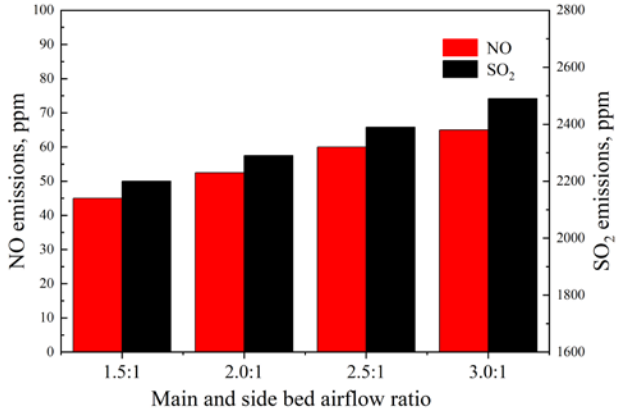

Fig. 15. Emissions of NO and SO_2 at different air distribution volumes in the main bed and side beds.

5. Conclusions

This study reveals that enhanced particle recirculation behavior, achieved by optimizing operational parameters such as a low excess air coefficient and a specific main/side bed airflow ratio in high-low differential velocity circulating fluidized beds, is crucial for achieving efficient fuel combustion and deep NOx suppression. The CPFD-predicted particle back-mixing correlates strongly with NO_X suppression efficiency. In the present study, the combustion characteristics in a 65-t/h high-low differential velocity CFB boiler were numerically simulated. Different excess air ratios and air volume ratios were considered to obtain the best working conditions. Based on the obtained results and analyses, the main conclusions can be summarized as follows:

1. This study demonstrates that the unique structural design of the high-low differential velocity circulating fluidized bed induces intense particle remixing. This hydrodynamic characteristic serves as the key intrinsic mechanism for achieving synergistic enhancement of efficient combustion and low pollutant emissions. Simulation results indicate that a moderate excess air coefficient (a = 1.10) maximizes this remixing effect.
2. Pyrolytic HCN and NH_3 peak near the feed ports and then decrease along the furnace height. Similarly, N_2O and NO concentrations also show peak values near the feeding zone under all tested excess air ratios.
3. Condition comparisons reveal that an excess air ratio of 1.10 promotes intense particle back-mixing and efficient combustion. Furthermore, at this optimal excess air ratio, the air volume ratio between the main bed and side beds significantly influences NO_x and SO_2 emissions, with a ratio of 1.5:1 yielding the lowest emissions.

Data availability statement

All data generated or analyzed during this study are contained within the article.

Acknowledgments

The authors appreciate the support of the Jilin Provincial Science and Technology Development Program (20200403162SF) and Jiangxi Jianglian Heavy Industry Group Co., Ltd. The publication costs of this article were partially covered by the Estonian Academy of Sciences.

References

1. Qing, W., Liu, H., Bai, J., Qin, H., Yang, W. Application of high-low bed CFB combustion technology to oil shale combustion. *Oil Shale*, 2013, **30**(2), 147–156. https://doi.org/10.3176/oil.2013.2.05
2. Wang, Q., Xiao, J. B., Liu, H. P. 2D CFD simulation of hydrodynamics of the dense zone of a 65 t/h high-low bed CFB. *Advanced Materials Research*, 2012, **614–615**, 596–599. https://doi.org/10.4028/www.scientific.net/AMR.614-615.596
3. Zhao, P. (P.), O'Rourke, P. J., Snider, D. Three-dimensional simulation of liquid injection, film formation and transport, in fluidized beds. *Particuology*, 2009, **7**(5), 337–346. https://doi.org/10.1016/j.partic.2009.07.002
4. O'Rourke, P. J., Zhao, P. (P.), Snider, D. A model for collisional exchange in gas/liquid/solid fluidized beds. *Chemical Engineering Science*, 2009, **64**(8), 1784–1797. https://doi.org/10.1016/j.ces.2008.12.014
5. Snider, D. M., Clark, S. M., O'Rourke, P. J. Eulerian–Lagrangian method for three-dimensional thermal reacting flow with application to coal gasifiers. *Chemical Engineering Science*, 2011, **66**(6), 1285–1295. https://doi.org/10.1016/j.ces.2010.12.042
6. O'Rourke, P. J., Snider, D. M. An improved collision damping time for MP-PIC calculations of dense particle flows with applications to polydisperse sedimenting beds and colliding particle jets. *Chemical Engineering Science*, 2010, **65**(22), 6014–6028. https://doi.org/10.1016/j.ces.2010.08.032
7. Abbasi, A., Ege, P. E., de Lasa, H. I. CPFD simulation of a fast fluidized bed steam coal gasifier feeding section. *Chemical Engineering Journal*, 2011, **174**(1), 341–350. https://doi.org/10.1016/j.cej.2011.07.085
8. Loha, C., Chattopadhyay, H., Chatterjee, P. K. Three dimensional kinetic modeling of fluidized bed biomass gasification. *Chemical Engineering Science*, 2014, **109**, 53–64. https://doi.org/10.1016/j.ces.2014.01.017
9. Ma, Q., Lei, F., Xiao, Y. Numerical analysis of operating conditions for establishing high-density circulating fluidized bed by CPFD method. *Powder Technology*, 2018, **338**, 446–457. https://doi.org/10.1016/j.powtec.2018.07.012
10. Tu, Q., Wang, H. CPFD study of a full-loop three-dimensional pilot-scale circulating fluidized bed based on EMMS drag model. *Powder Technology*, 2018, **323**, 534–547. https://doi.org/10.1016/j.powtec.2017.09.045
11. Chen, C., Werther, J., Heinrich, S., Qi, H.-Y., Hartge, E.-U. CPFD simulation of circulating fluidized bed risers. *Powder Technology*, 2013, **235**, 238–247. https://doi.org/10.1016/j.powtec.2012.10.014
12. Liu, H., Li, J., Wang, Q. Three-dimensional numerical simulation of the co-combustion of oil shale retorting solid waste with cornstalk particles in a circulating fluidized bed reactor. *Applied Thermal Engineering*, 2018, **130**, 296–308. https://doi.org/10.1016/j.applthermaleng.2017.10.107
13. Liu, H., Li, J., Wang, Q. Simulation of gas–solid flow characteristics in a circulating fluidized bed based on a computational particle fluid dynamics

model. *Powder Technology*, 2017, **321**, 132–142. https://doi.org/10.1016/j.powtec.2017.07.040

14. Wang, Q., Yang, H., Wang, P., Lu, J., Liu, Q., Zhang, H. et al. Application of CPFD method in the simulation of a circulating fluidized bed with a loop seal, part I—determination of modeling parameters. *Powder Technology*, 2014, **253**, 814–821. https://doi.org/10.1016/j.powtec.2013.11.041
15. Shi, X., Lan, X., Liu, F., Zhang, Y., Gao, J. Effect of particle size distribution on hydrodynamics and solids back-mixing in CFB risers using CPFD simulation. *Powder Technology*, 2014, **266**, 135–143. https://doi.org/10.1016/j.powtec.2014.06.025
16. Lan, X., Shi, X., Zhang, Y., Wang, Y., Xu, C., Gao, J. Solids back-mixing behavior and effect of the mesoscale structure in CFB risers. *Industrial & Engineering Chemistry Research*, 2013, **52**(34), 11888–11896. https://doi.org/10.1021/ie3034448
17. Yan, J., Lu, X., Xue, R., Lu, J., Zheng, Y., Zhang, Y. et al. Validation and application of CPFD model in simulating gas-solid flow and combustion of a supercritical CFB boiler with improved inlet boundary conditions. *Fuel Processing Technology*, 2020, **208**, 106512. https://doi.org/10.1016/j.fuproc.2020.106512
18. Shen, X., Jia, L., Wang, Y., Guo, B., Fan, H., Qiao, X. et al. Study on dynamic characteristics of residual char of CFB boiler based on CPFD method. *Energies*, 2020, **13**(22), 5883. https://doi.org/10.3390/en13225883
19. Auzerais, F. M., Jackson, R., Russel, W. B. The resolution of shocks and the effects of compressible sediments in transient settling. *Journal of Fluid Mechanics*, 1988, **195**, 437–462. https://doi.org/10.1017/S0022112088002472
20. Snider, D. M. An incompressible three-dimensional multiphase particle-in-cell model for dense particle flows. *Journal of Computational Physics*, 2001, **170**(2), 523–549. https://doi.org/10.1006/jcph.2001.6747
21. Jalali, P., Hyppänen, T. Momentum transport between two granular phases of spherical particles with large size ratio: two-fluid model versus discrete element method. *Powder Technology*, 2015, **273**, 13–18. https://doi.org/10.1016/j.powtec.2014.12.026
22. Lanza, A., Islam, M. A., de Lasa H. CPFD modeling and experimental validation of gas–solid flow in a down flow reactor. *Computers & Chemical Engineering*, 2016, **90**, 79–93. https://doi.org/10.1016/j.compchemeng.2016.04.007
23. Snider, D. M., Clark, S. M., O'Rourke, P. J. Eulerian–Lagrangian method for three-dimensional thermal reacting flow with application to coal gasifiers. *Chemical Engineering Science*, 2011, **66**(6), 1285–1295. https://doi.org/10.1016/j.ces.2010.12.042
24. de Souza-Santos, M. L. Comprehensive modelling and simulation of fluidized bed boilers and gasifiers. *Fuel*, 1989, **68**(12), 1507–1521. https://doi.org/10.1016/0016-2361(89)90288-3
25. Goel, S. K., Morihara, A., Tullin, C. J., Sarofim, A. F. Effect of NO and O_2 concentration on N_2O formation during coal combustion in a fluidized-bed combustor: modeling results. *Symposium (International) on Combustion*, 1994, **25**(1), 1051–1059. https://doi.org/10.1016/S0082-0784(06)80743-5

26. Liu, H., Feng, B., Lu, J., Zheng, C. Coal property effects on N_2O and NO_x formation from circulating fluidized bed combustion of coal. *Chemical Engineering Communications*, 2005, **192**(11), 1482–1489. https://doi.org/10.1080/009864490896043
27. Kilpinen, P., Kallio, S., Konttinen, J., Barišić, V. Char-nitrogen oxidation under fluidised bed combustion conditions: single particle studies. *Fuel*, 2002, **81**(18), 2349–2362. https://doi.org/10.1016/S0016-2361(02)00176-X
28. Shi, X., Wu, Y., Lan, X., Liu, F., Gao, J. Effects of the riser exit geometries on the hydrodynamics and solids back-mixing in CFB risers: 3D simulation using CPFD approach. *Powder Technology*, 2015, **284**, 130–142. https://doi.org/10.1016/j.powtec.2015.06.049
29. Zhong, W., Xie, J., Shao, Y., Liu, X., Jin, B. Three-dimensional modeling of olive cake combustion in CFB. *Applied Thermal Engineering*, 2015, **88**, 322–333. https://doi.org/10.1016/j.applthermaleng.2014.10.086